NSU3D Results for the Fourth AIAA Drag Prediction Workshop

Dimitri Mavriplis [*]

Mike Long [†]

Department of Mechanical Engineering

University of Wyoming, Laramie, Wyoming, 82072-3295

Simulation results for the Common Research Model (CRM) transport aircraft performed for the fourth Drag Prediction Workshop (DPW4) using the unstructured computational fluid dynamics code NSU3D are presented. The solution algorithms employed in NSU3D for this study are described along with examples of convergence history. The CRM aircraft configuration used for the workshop consists of the wing, body, and horizontal tail with no vertical tail or engine nacelles. The computational meshes for this study were provided by NASA Langley and were prepared with the VGrid package. A complete lift-drag polar is produced in NSU3D on a baseline mesh along with additional runs on refined and coarsened meshes to assess sensitivity to grid resolution. The effect of horizontal tail angle on the drag polar is investigated and the trimmed drag polar calculated. A range of Mach number values are evaluated and the drag polar and drag rise curves presented. The effect of Reynolds number is assessed by comparing computed results at Reynolds numbers of 5 million and 20 million.

I.   Introduction

Starting in 2001, the AIAA Applied Aerodynamics Technical Committee has sponsored several Drag Prediction Workshops (DPW) in order to provide a form for the assessment of the state-of-the-art in Computational Fluid Dynamics (CFD) tools for determining both absolute and incremental drag on generic transonic transport aircraft configurations. The fourth Drag Prediction Workshop (DPW4) was held in San Antonio, TX, in June 2009 and was the first workshop to make use of the Common Research Model (CRM). The CRM is a wind-body-horizontal (tail) configuration which was developed by NASA's Subsonic Fixed Wing (SFW) Aerodynamics Technical Working Group (TWG) in collaboration with the DPW Organizing Committee. The CRM configuration is representative of a contemporary high-performance transonic commercial transport aircraft. A detailed description of the development of the CRM is given by Vassberg.[1]

As with previous workshops, DPW4 placed considerable weight on assessing the impact of discretization error through a mandatory grid convergence study. However, an important new aspect of the fourth workshop was a downwash study and the prediction of trim drag, made possible by the presence of the horizontal tail on the CRM. Previous workshops have concentrated on assessing the scatter between the various computationally generated results, although experimental data has also been available in most cases for comparison with CFD results. For DPW4, the CRM geometry had been defined but not tested and thus DPW4 consisted of a truly blind CFD predictive test. Subsequently, the CRM has been tested in the NASA Langley National Transonic Facility (NTF) and the NASA Ames 11 ft transonic tunnel in 2010, and results are reported in reference.[2] However, at the time of writing, experimental results were not available for inclusion in the current paper.

The objective of this paper is to document the results obtained at the fourth Drag Prediction Workshop based on the CRM using the NSU3D unstructured mesh Reynolds-averaged Navier-Stokes solver. The NSU3D code has been a participant in all four DPW workshops since 2001,[3–6] and is currently a participant

---

[*]Professor, Associate Fellow, email: mavripl@uwyo.edu

[†]Applications Engineer, Member, email: mlong16@uwyo.edu

American Institute of Aeronautics and Astronautics

in the High Lift Prediction Workshop, to be held in Chicago, IL, in June 2010.[7] The NSU3D solver has also been involved in various DPW follow-on studies, including comparisons with other solvers,[8–10] sensitivity studies, and extensive grid refinement studies.[11, 12]

The NSU3D solver is described briefly in the next section. In section III, a description of the CRM aircraft geometry used as the subject of the workshop is given. This is followed by a description of the various unstructured meshes used for the calculations reported in this paper in section V. The results obtained with the NSU3D solver are then described and discussed in Section VI, and conclusions are given in Section VII.

II.   Solver Description

The NSU3D code is an unstructured mesh multigrid Reynolds-averaged Navier-Stokes (RANS) solver for high-Reynolds number external aerodynamic applications. The NSU3D discretization employs a vertex-based approach, where the unknown fluid and turbulence variables are stored at the vertices of the mesh, and fluxes are computed on faces delimiting dual control volumes, with each dual face being associated with a mesh edge. This discretization operates on hybrid mixed-element meshes, generally employing prismatic elements in highly stretched boundary layer regions, and tetrahedral elements in isotropic regions of the mesh away from the aircraft surfaces. A single edge-based data-structure is used to compute flux balances across all types of elements. The convective terms are discretized as central differences with added matrix dissipation. Second-order accuracy is achieved by formulating these dissipative terms as an undivided bi-harmonic operator, which is constructed in two passes of a nearest-neighbor Laplacian operator. In the matrix form, this dissipation is similar to that produced by a Riemann solver gradient-based reconstruction scheme, and is obtained by replacing the difference in the reconstructed states on each side of the control volume interface by the undivided differences along mesh edges resulting from the biharmonic operator construction. These differences are then multiplied by the characteristic matrix to obtain the final dissipation terms. A Roe upwind scheme using least-squares gradient reconstruction is also available in the NSU3D solver.

The baseline NSU3D discretization employs a finite-difference scheme to approximate the thin-layer form of the viscous terms for the Navier-Stokes equations, although this is done in a multidimensional fashion, by computing a Laplacian of the velocity field.[13] The main approximation in this approach is the omission of the cross-derivative viscous terms, and the assumption of a locally constant viscosity. The discretization of the full Navier-Stokes terms has also been implemented. This is achieved by first computing gradients of the flow variables at the grid vertices, using an edge-based loop, and then using a second edge loop to assemble the viscous flux balance at each vertex, based on these gradients. This approach results in an extended neighbor-of-neighbor stencil, which is less accurate than a nearest-neighbor stencil. However, a nearest-neighbor stencil discretization of second derivatives on mixed element meshes requires the use of a cell data-structure, while the current approach relies exclusively on the edge-data structure. In order to improve the accuracy and stability of this discretization, a hybrid approach is adopted, where the second derivatives in the directions aligned with the incident mesh edges are computed using a nearest-neighbor stencil on the edges, while the remaining terms are computed using the extended stencil using the two pass approach.

NSU3D incorporates the single equation Spalart-Allmaras turbulence model,[14] as well as a standard $k-\omega$ two-equation turbulence model,[15] and the two-equation shear-stress transport (SST) model due to Menter.[16] Facilities for specified transition location based on the surface geometry are provided. While this capability was employed in DPW II,[4, 10] the cases for DPW4 were all run fully turbulent.

The basic time-stepping scheme in NSU3D consists of a three stage explicit multistage scheme. Convergence is accelerated by a local block-Jacobi preconditioner in regions of isotropic grid cells. In boundary layer regions, where the grid is highly stretched, a line preconditioner is employed to relieve the stiffness associated with the mesh anisotropy.[17] An agglomeration multigrid algorithm is used to further enhance convergence to steady-state.[13, 18] The Jacobi and line preconditioners are used to drive the various levels of the multigrid sequence, resulting in a rapidly converging solution technique. NSU3D includes a C_L driver capability that allows convergence to a fixed lift coefficient value. Based on user defined inputs, the code periodically adjusts the incidence during the computation based on the current C_L value until the prescribed C_L value is achieved at convergence. Convergence can be driven either by a prescribed lift condition (C_L driver) or a prescribed z-force condition (C_Z driver).

Figure 1(a) illustrates a typical convergence history for a transonic aircraft configuration using three meshes of increasingly finer resolution. The solver is generally run 500 multigrid cycles, and up to 1000

American Institute of Aeronautics and Astronautics

cycles for more stringent cases with larger amounts of separated flow. The convergence is seen to be similar for all three grids, with only slight decrease in the convergence rate as the grid resolution is increased. This is a property of the multigrid scheme, which is designed as an optimal solver to deliver convergence rates which are independent of the number of degrees of freedom.

The multigrid solver has been implemented as a non-linear (FAS) solver, and more recently a linear single grid and multigrid solver has been implemented, primarily for time dependent calculations, where initial convergence transients are avoided due to the availability of previous time step information. In this approach, multiple linear sweeps using a point or line-implicit Jacobi approach are used to converge the linear problem before updating the outer non-linear iterations. For cases at the edge of the flight envelope where non-linear multigrid has been found to be problematic, the linear solver can often be used to provide tighter convergence tolerances.

NSU3D employs a dual level parallelization strategy invoking the MPI interface for interprocessor communication across distributed memory nodes, with the ability to use OpenMP constructs for inter-node shared memory parallelism. NSU3D has been shown to scale well on massively parallel computer architectures using up to 4000 cores.[19] The results reported in this paper have been run on the NASA Pleiades machine, using MPI exclusively and using from 32 to 256 cores.

NSU3D also has been interfaced to a far-field drag decomposition method which provides a breakdown of aerodynamic drag into induced, entropy, and spurious components.[20, 21] By subtracting out the spurious components, better estimates of physical drag can be obtained on coarser grids.
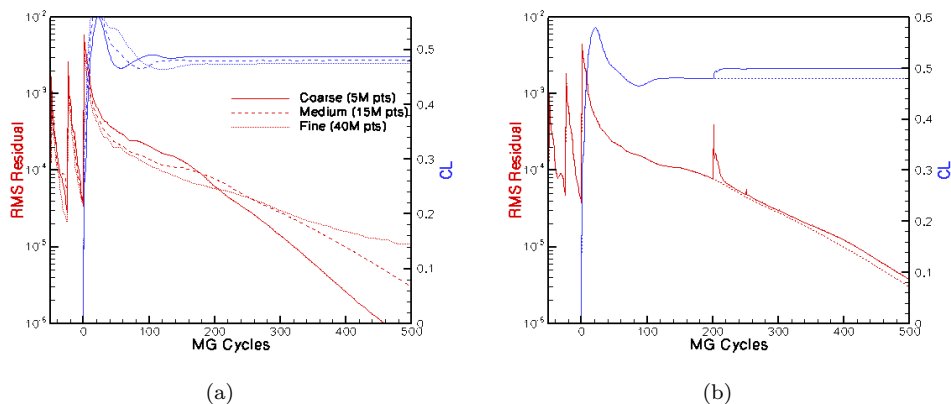

Figure 1. (a): Multigrid convergence rate achieved on transonic Wing-Body configuration from DPW3

III.   Common Research Model Description

The CRM is a generic transport aircraft configuration that was developed by NASA in collaboration with the DPW Organizing Committee for current and future aerodynamic research purposes. The CRM is a complete geometry that includes wing-body-tail as well as nacelles and pylons. For the DPW4 study, only clean wing (no nacelles/pylons) were considered. Figure 2 provides an illustration of the CRM geometry with and without nacelles/pylons. The CRM was designed for a cruise condition of Mach=0.85 and $C_L = 0.5$ at a nominal altitude of 37,000 ft. The wing planform has an aspect ratio of 9.0 and a leading edge sweep of 35°. The upper surface pressure recovery over the outboard wing has been designed intentionally to be aggressively adverse over the last 10-15% local chord, in order to weaken the health of the upper surface boundary layer near the trailing edge region. This provides a fairly controlled trailing edge separation, the prediction of which constitutes one of the workshop objectives. A detailed description of the development of the CRM is given by Vassberg.[1]

In contrast with previous DPW workshops, the inclusion of the horizontal tail in the CRM geometry provides a basis for numerical investigations of trim drag prediction. The horizontal tail is defined by symmetric airfoil sections with 2.5^o of twist at the tip. The tail-fuselage intersection line defining the root airfoil section remains sealed against the fuselage as the horizontal tail rotates about its hinge line. For DPW4, four configurations where used: three configurations with horizontal tail settings of $iH = -2^o$,

American Institute of Aeronautics and Astronautics

$iH = 0^o$, and $iH = 2^o$, respectively, and a tail off (wing-body only) configuration.
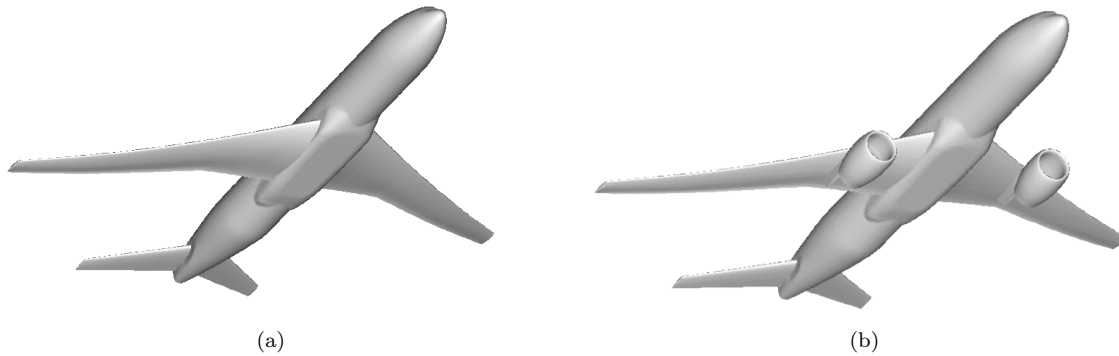

(a)   (b)

Figure 2. (a) NASA Common Research Model used for DPW4 and CRM model with engine nacelles

IV. Grid Generation

All of the grids used for this study were provided by NASA Langley and were created using the VGRIDns unstructured grid generator. Table 1 lists the node and cell counts for each grid. A total of seven different grids were used for these calculations. The baseline configuration consists of the wing-body-horizontal with a horizontal tail setting of 0°. A grid refinement study on this configuration required the generation of three progressively finer grids (referred to as coarse, medium and fine). An additional (fourth) mesh for this configuration was generated with resolution similar to the medium mesh mentioned above, but with tighter normal boundary layer spacings designed for simulations at a higher Reynolds number. An extra-fine mesh was also generated for this configuration but not used in the current calculations. A medium level resolution mesh was generated for each of the three other configurations ($-iH = 2^o$, $iH = -2^o$ horizontal tail settings, and tail off)

As with the previous workshops, a set of gridding guidelines has been produced and is summarized in Reference.[22] These grids have been made available on the DPW4 web site under the designation "LaRC Unstructured Node-Based". The meshing guidelines include a farfield boundary at 100 chord lengths away, a normal spacing at the wall of $y+ \leq 1.0$ for the coarsest grids, with progressively smaller spacings on the finer grids, chordwise spacings at the wing leading and trailing edges of approximately 0.1% chord on the coarse mesh, and spanwise spacings of 0.1% at the wing root and tip on the coarsest mesh as well. A resolution of 8, 12, and 16 cells across the blunt trailing edge of the wing was specified for the coarse, medium and fine grids respectively, and the overall size of the grids was targeted to grow by a factor of three when going from coarse to medium, and medium to fine. Care was taken to generate corresponding coarse, medium and fine meshes with self-similar resolution distributions, such that these grids can be considered to be of the same "family" for grid convergence studies.[22] The medium grid was specified to be representative of the resolution level used in current industrial production runs.

NSU3D supports hybrid meshes with different element types and the preferred mode of operation is to employ prismatic elements in boundary layer regions. Therefore, the fully tetrahedral meshes generated by VGRIDns are transformed into hybrid prismatic-tetrahedral meshes in a preprocessing phase, by merging triplets of tetrahedra in the boundary layer regions into prismatic elements prior to NSU3D computations. This process also results in a small number of pyramidal elements in regions where exposed prismatic quadarilateral faces interface with tetrahedral elements. The final hybrid-element mesh characteristics are listed in Table 2. Figure 3 shows the relative mesh resolution over the wing planform for the family of NASA provided grids, while Figure 4 illustrates the mesh resolution at the wing trailing edge.

Table 1. Descriptions of NASA provided grids. Boundary layer spacings are in inches.

Grid Name	Nodes	Tetras	y+	BL Spacing	Notes
dpw-wb0_med-8Mn_5	8,206,796	48,397,830	2/3	0.000985	Tail off, medium, Re=5M
dpw_wbt0_crs-3.6Mn_5	3,661,747	21,600,451	1.0	0.001478	Tail 0°, coarse, Re=5M
dpw-wbt0_med-10Mn_5	10,226,105	60,346,540	2/3	0.000985	Tail 0°, medium, Re=5M
dpw-wbt0_fine-35Mn_5	35,967,824	212,222,168	4/9	0.000657	Tail 0°, fine, Re=5M
dpw-wbt2dn_med-10Mn_5	10,029,456	59,188,129	2/3	0.000985	Tail -2°, medium, Re=5M
dpw-wbt2up_med-10Mn_5	10,047,721	59,295,849	2/3	0.000985	Tail +2°, medium, Re=5M
dpw-wbt0_med-11Mn_20	11,281,422	66,666,252	2/3	0.000273	Tail 0°, medium, Re=20M

Table 2. Descriptions grids after merging of boundary layer tetrahedra into prismatic elements for NSU3D

Grid Name	Nodes	Tetras	Prisms	Pyramids
dpw-wb0_med-8Mn_5	8,250,973	15,744,248	10,899,243	88,369
dpw_wbt0_crs-3.6Mn_5	3,697,406	3,961,757	5,891,445	71,327
dpw-wbt0_med-10Mn_5	10,288,154	15,052,086	15,118,827	124,109
dpw-wbt0_fine-35Mn_5	36,081,758	76,902,242	45,144,640	227,838
dpw-wbt2dn_med-10Mn_5	10,090,346	14,511,390	14,912,511	121,828
dpw-wbt2up_med-10Mn_5	10,109,274	14,515,625	14,947,247	123,124
dpw-wbt0_med-11Mn_20	11,336,666	15,436,245	17,095,161	110,3072

(a) Coarse (b) Medium (c) Fine
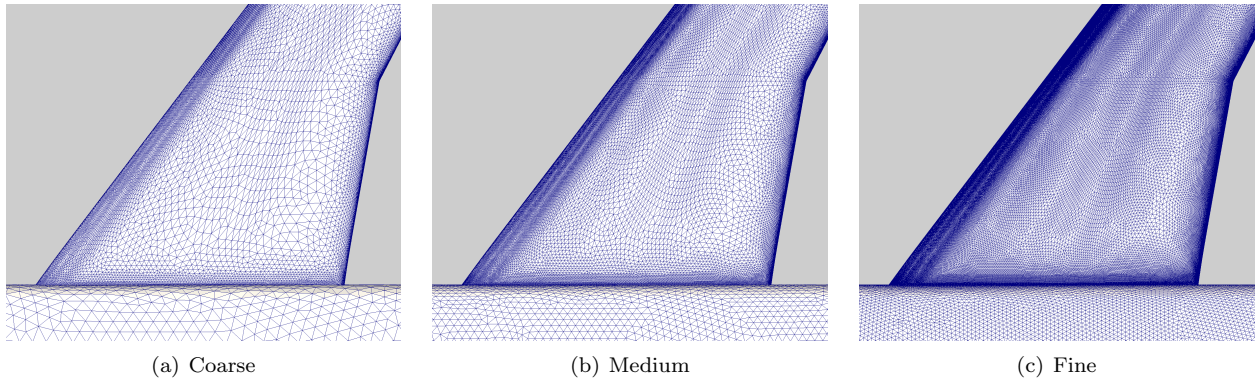
Figure 3. Comparison of wing planform mesh resolution for NASA provided grids

(a) Coarse (b) Medium (c) Fine
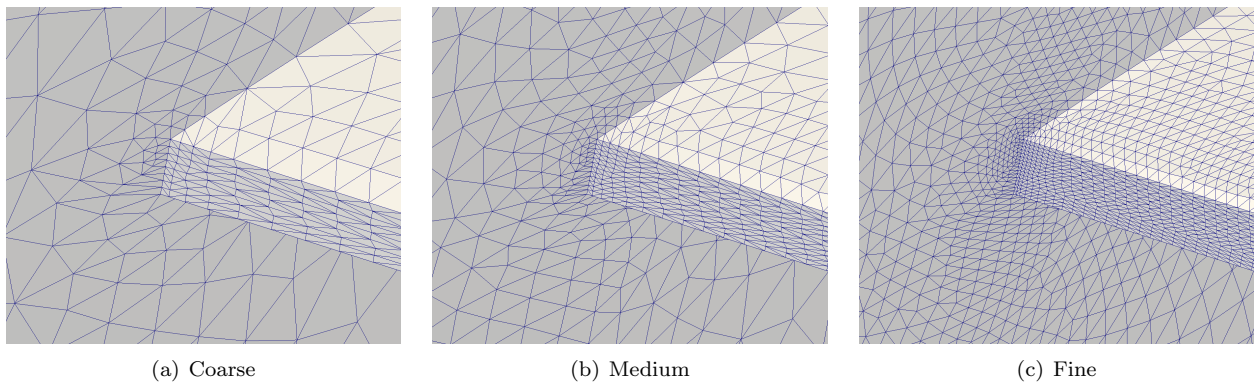
Figure 4. Comparison of wing trailing edge mesh resolution for NASA provided grids

American Institute of Aeronautics and Astronautics

V. Results

A. Case 1a: Grid Convergence Study

The first test case (required) for DPW4 consists of a grid convergence study on the wing-body-horizontal configuration with a horizontal tail setting of $iH = 0^o$. The test case conditions are Mach=0.85, C_L=0.5, and Re = 5 million. The flow field was computed for these conditions using the C_L driver capability in NSU3D on the self-similar coarse, medium and fine meshes for this configuration (see Table 2) containing 3.7 million, 10 million, and 36 million points respectively. The computed values of the drag and moment coefficients and the incidence angle required to achieve the prescribed lift condition are plotted in Figures 5 and 6 versus the *grid index*, defined as the inverse of the number of grid points to the $\frac{2}{3}$ power, with the understanding that for a family of self-similar coarse to fine grids, this quantity should be representative of the average cell size h to the second power. Thus, straight-line plots in these figures are indicative of second-order accurate spatial convergence and extrapolation to the y-axis provides an estimate of the values which would be predicted in the presence of infinite grid resolution.

Figure 5 depicts the total computed drag coefficients at fixed $C_L = 0.5$ as a function of the grid resolution index. A slightly lower slope is observed between the medium and fine grids compared to the coarse to medium slope, indicating that the coarse mesh is most likely not in the asymptotic range of convergence for discretization error. Extrapolating to the y-axis gives an infinite resolution drag of 0.0268, which is very close to the median of the collective structured and unstructured mesh results reported in the workshop.[23]
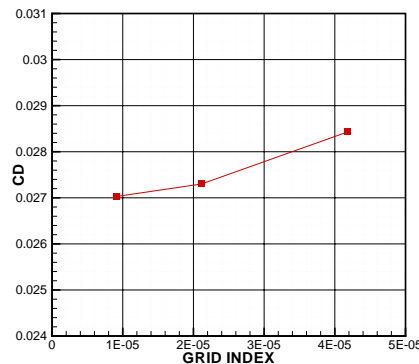

(a)

Figure 5. Grid convergence plots on CRM with tail at $iH = 0^o$ for surface integrated total drag coefficient for $C_L = 0.5$ and Re=5 million case

.

The far-field drag integration approach[20, 21] which allows for the decomposition of the drag into induced, entropy and spurious components, was applied to the results on the coarse and medium meshes. A total of 20 counts and 8 counts of spurious drag was reported on the coarse and medium meshes respectively, which when subtracted from the surface integrated values obtained on these meshes, correlates well with the estimate of infinite resolution drag given previously.

The angle of attack required to match the $C_L = 0.5$ condition, and obtained as part of the iterative solution procedure using the C_L driver, is plotted versus the grid resolution index in Figure 6(a). The incidence increases slightly between the medium and fine grids, producing a value of 2.39 degrees on the fine mesh.

Figure 6(b) depicts the pitching moment coefficient computed on all three grids as a function of the grid resolution index. In this case, a relatively straight line is observed, indicative of second-order accuracy. The reported moment values are within the scatter band of the core group of solutions reported in the workshop, although the fine grid value is one of the larger moment values reported by the core group of solutions in the workshop.

An investigation of the sensitivity of these grid convergence results to discretization schemes in the NSU3D solver was also undertaken. The same condition was recalculated on the medium grid using the
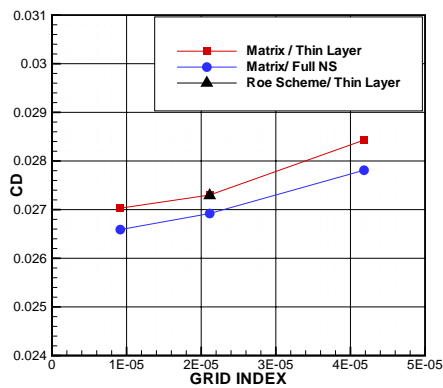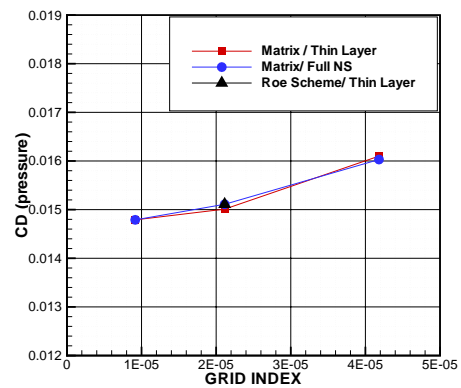
American Institute of Aeronautics and Astronautics
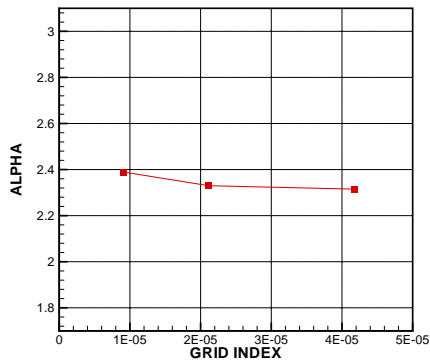
(a)
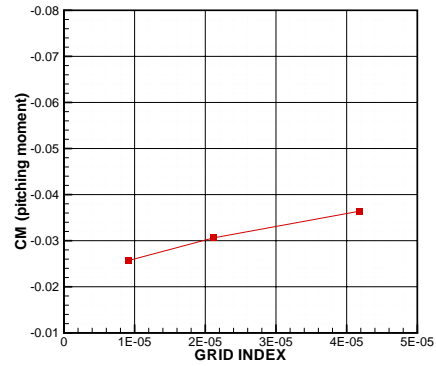
(b)

Figure 6. Grid convergence plots on CRM with tail at $iH = 0^o$ **for (a) Incidence and (b) Pitching moment for** $C_L = 0.5$ **and Re=5 million case**

.

(a)

(b)

Figure 7. Grid convergence of different discretizations on CRM with tail at $iH = 0^o$ **for (a) Total Drag Coefficient and (b) Pressure Drag Coefficient for** $C_L = 0.5$ **and Re=5 million case**
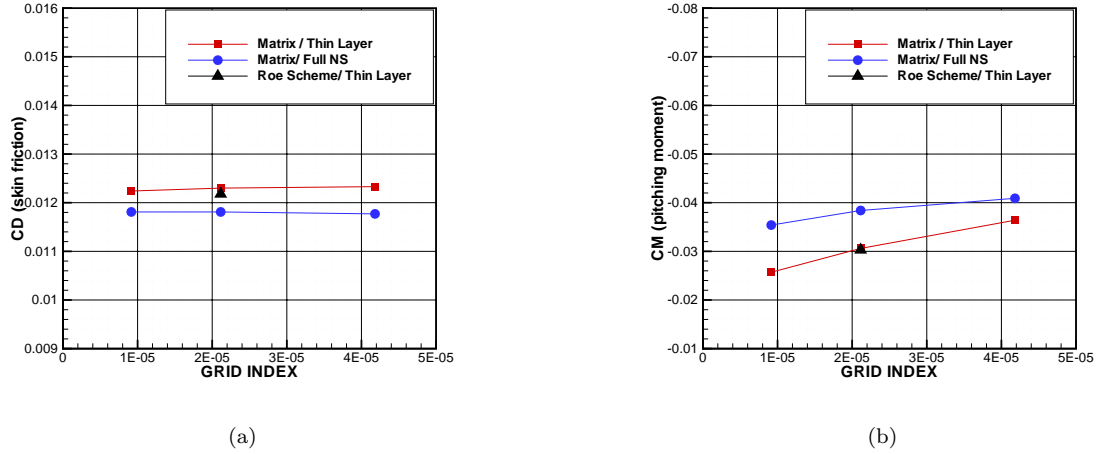
.

American Institute of Aeronautics and Astronautics

Figure 8. Grid convergence of different discretizations on CRM with tail at $iH = 0^o$ for (a) Friction Drag Coefficient and (b) Pitching moment for $C_L = 0.5$ and Re=5 million case
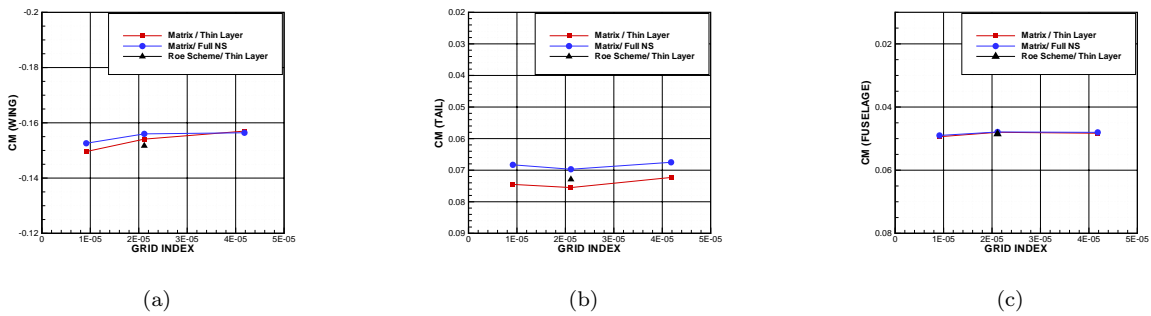
.

Figure 9. Component-wise grid convergence of pitching moment coefficient for different discretizations on CRM with tail at $iH = 0^o$ for (a) wing, (b) tail, and (c) fuselage for $C_L = 0.5$ and Re=5 million case

.

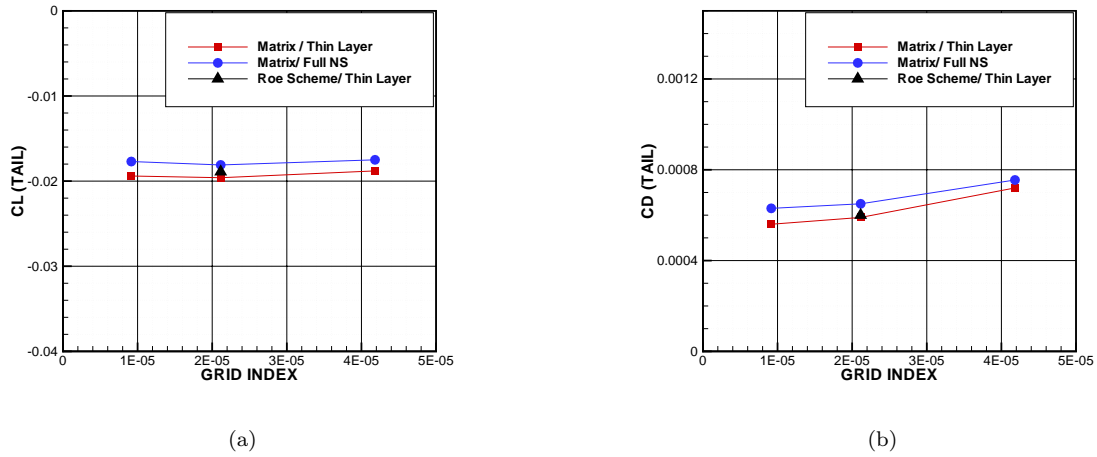American Institute of Aeronautics and Astronautics

(a)

(b)

Figure 10. Grid convergence of different of tail forces on CRM with tail at $iH = 0^o$ for (a) Lift Coefficient and (b) Drag Coefficient for $C_L = 0.5$ and Re=5 million case
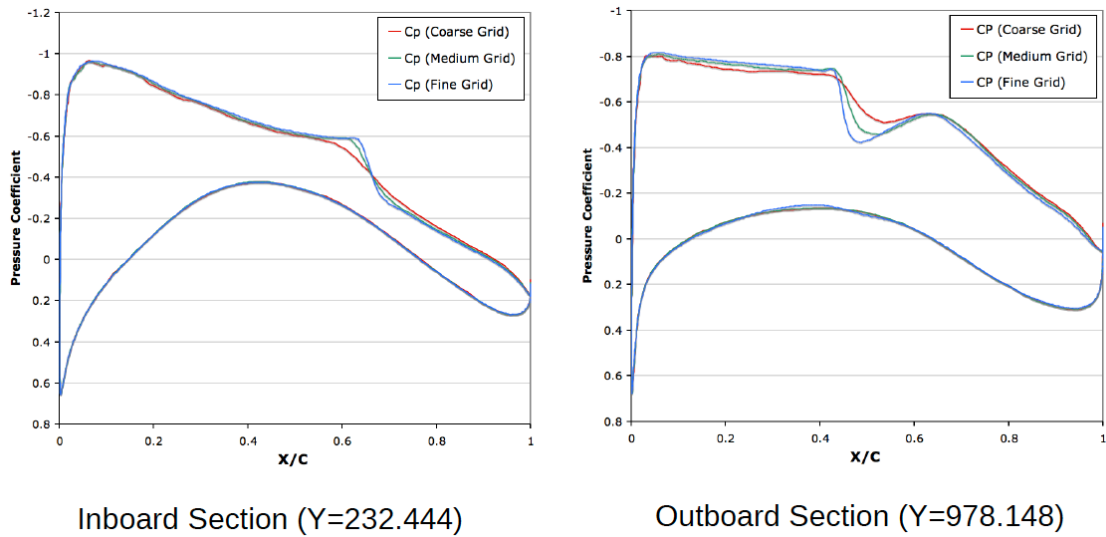
.

Inboard Section (Y=232.444)

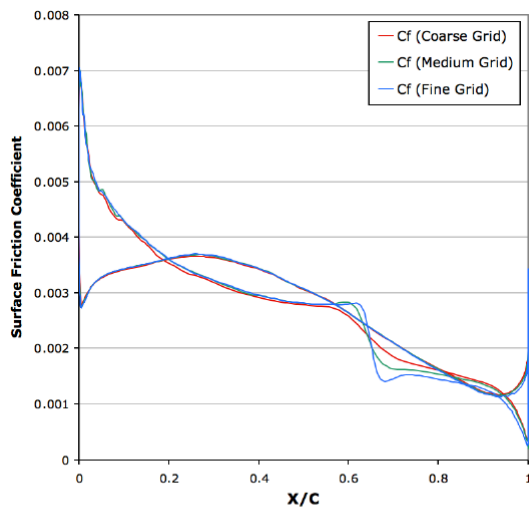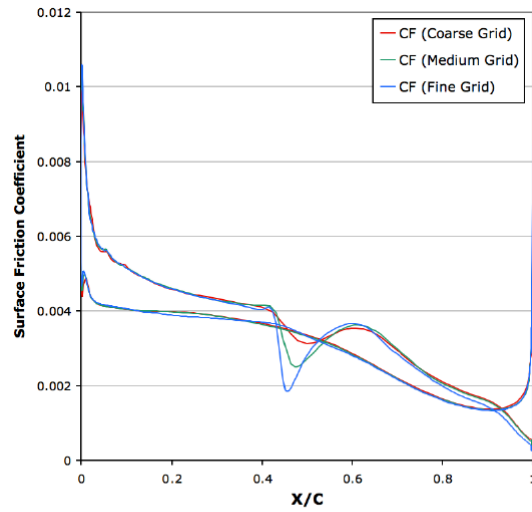Outboard Section (Y=978.148)

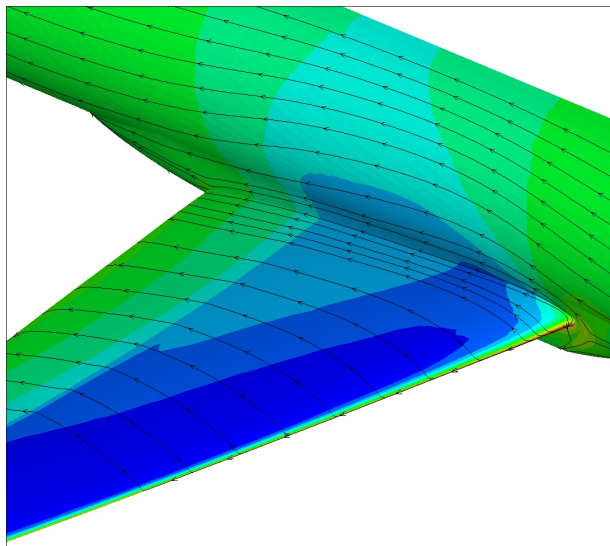**Figure 11. Sensitivity of surface pressure to grid size**
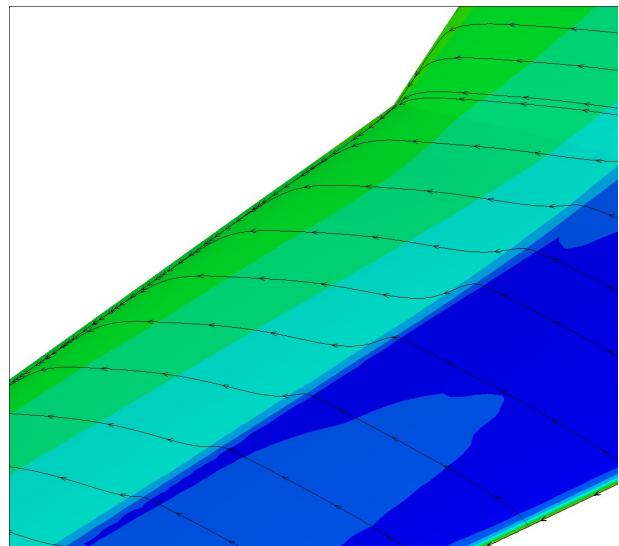
Inboard Section (Y=232.444)

Outboard Section (Y=978.148)

Figure 12. Sensitivity of surface skin friction to grid size

(a)

(b)

Figure 13. Computed surface oil flow patterns on wing and close up showing small region of trailing edge separation for CRM configuration with tail at $iH = 0^o$ at Mach=0.85 $C_L = 0.5$ and Re= 5 million

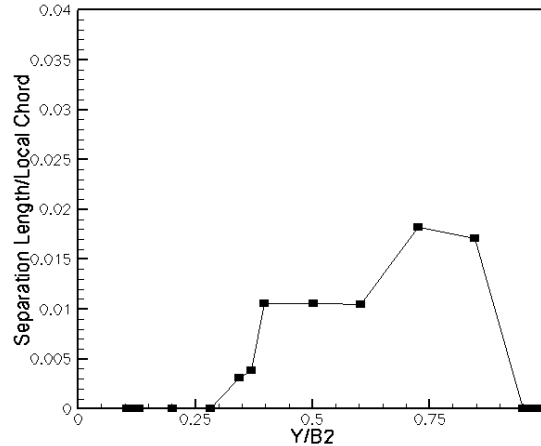American Institute of Aeronautics and Astronautics

Figure 14. Extent of separation along wing trailing edge as function of span location on medium resolution mesh for CRM configuration with tail at $iH = 0^o$ **at Mach=0.85** $C_L = 0.5$ **and Re= 5 million**

Roe upwind scheme with least-squares gradient reconstruction, and the baseline matrix dissipation scheme with full Navier-Stokes terms. The results of this study are depicted in Figures 7 and 8. The Roe scheme results were found to be very close to the original calculations reported above using the baseline matrix dissipation scheme, and therefore were only computed on the medium grid. The full Navier-Stokes results produced small but noticeable changes on the medium grid and were therefore applied to the complete grid convergence study. In Figure 7(a), the drag computed using the full Navier-Stokes terms is seen to be consistently about 4 counts lower than the drag obtained with the baseline scheme, while the Roe scheme on the medium grid gave essentially identical drag compared to the baseline scheme. The grid convergence of the separate pressure drag and friction drag components is depicted in Figures 7(b) and 8(a). The pressure drag is essentially the same for all three discretizations and the difference in total drag between thin layer and full Navier-Stokes terms is seen to come from an equivalent difference in skin friction drag. The shape of the pressure drag curve follows that of the total drag convergence curve and is close to the median values reported by the workshop collective results. The friction drag is relatively constant across all three grids and agrees well with the collective results from the workshop. In Figure 8(b) the grid convergence of the pitching moments for the various discretization schemes is compared. Again, the Roe scheme produces essentially the same pitching moment as the baseline scheme on the medium grid. However, the full Navier-Stokes discretization produces somewhat more negative pitching moment values on the medium and fine meshes. The values produced by the full Navier-Stokes discretization are closer to the median values reported by the workshop collective results. In general, the scatter in moment values reported by the collective workshop solutions is larger than the scatter in the drag values, and larger than the moment scatter seen in previous workshops. This has led to speculation that the downwash effects on the tail, which may be more sensitive to grid resolution effects, are responsible for the increased moment variations. On the one hand, we note that the absolute moment values in this particular case are relatively small (i.e. 4 to 5 times smaller than for the DLR-F6 in DPW3) which has a magnifying effect on the ratio of scatter to mean value. In order to further examine the contributions to the moment variations, the component (wing, fuselage, tail) contributions to total pitching moment are shown in Figure 9 as a function of the grid refinement index. From these figures, it can be surmised that the changes in the pitching moment between the thin layer and full Navier-Stokes results are due to similar contributions from the wing and tail, with almost no contribution from the fuselage. Furthermore, the tail differences are relatively insensitive to grid resolution, as they appear as a bias between the two schemes that does not change significantly as the mesh is refined. Thus it appears that the downwash at the tail is captured adequately with the medium grid and the difference between the two schemes may be due more to a small change in the amount of trailing edge separation on the wing, and the indirect effect this may have on the tail. In Figure 10 the computed lift and drag values on the horizontal tail show similar trends, with a relatively constant bias between the two schemes over the three different grids. The influence of the viscous term discretization on these quantities is surprising, since previous computations showed little

American Institute of Aeronautics and Astronautics

sensitivity to the viscous term formulation.[6,12] However, the absolute differences are still relatively small (for example there is less than 1 count of drag difference in tail values of Figure 10(b)).

In Figure 11, the computed surface pressures at two stations on the wing are plotted for all three grids, using the baseline discretization. The principal trends with grid refinement correspond to a sharpening of the shock wave on the upper surface of the wing. A similar plot is given in Figure 12 for the skin friction, illustrating the relative insensitivity of these values to additional grid refinement.

Figure 13 illustrates the computed surface pressure and oil flow traces on the wing of the CRM, showing the shock structure and the small amount of trailing edge separation. Figure 14 provides a record of the separation location near the trailing edge of the wing plotted along the spanwise coordinate, for the three different meshes. A small region of trailing edge separation is observed, which reaches a maximum extent of roughly 2% local chord.

B. Case 1b: Downwash Study

The second mandatory test case for the workshop consisted of a downwash study in aircraft design. This represents a defining feature of the fourth workshop (DPW4) made possible by the presence of the horizontal tail on the CRM, compared to previous workshops where wing-body only configurations were considered (pylon/nacelles were considered in DPW2). The downwash study is performed by computing alpha sweeps at fixed Mach number on the CRM with three different horizontal tail settings: tail incidences of $iH = -2^o$, $iH = 0^o$, and $iH = 2^o$. Additionally, a sweep is performed with the CRM tail-off configuration. The trimmed condition is defined as the tail setting which produces a zero net pitching moment about the reference point. The values of the tail setting and force coefficients at the trimmed condition are obtained by interpolating the values from the three tail incidence sweeps. Since three tail incidences are used, a quadratic fit between these three data points can be used to determine the trimmed condition values. The trim drag penalty is then defined as the difference between the drag at the trimmed condition and the drag for the tail-off condition. The downwash angle at the tail is also defined as the overall tail incidence to the freestream flow (i.e. tail setting plus aircraft angle of attack) which results in the same overall lift as the tail-off configuration at a given freestream angle of attack.

Figure 15 depicts the drag polars for all five configurations (three tail settings, tail-off, and trimmed). For clarity, the tail-off and trimmed configuration polars are reproduced in Figure 15(b). The same polars are also plotted in Figure 16 in term of idealized profile drag, where the estimate of induced drag is subtracted from the total drag coefficient, enabling the use of expanded drag scales. The lowest drag is achieved for the tail-off configuration (except at the highest lift condition). The $iH = +2^o$ configuration produces drag values roughly 5 counts lower than the $iH = 0^o$ configuration, while the $iH = -2^o$ is about 20 counts higher. The trimmed drag polar produces drag values slightly higher than the $iH = 0^o$ configuration, with a drag increase of 4 counts over this configuration at $C_L = 0.5$.

Figure 17 depicts the C_L versus incidence curves for the same five configurations (including the trimmed configuration). The lift slope curve for the tail-off configuration is approximately $\frac{\partial C_L}{\partial \alpha} = 0.139$ per degree for the tail-off configuration and $\frac{\partial C_L}{\partial \alpha} = 0.149$ per degree for the wing-body-tail configurations, including the trimmed configuration. The C_L values are generally lower for the configurations with the tail compared to the tail-off configuration, and the lift curve break occurs between 3 and 4 degrees for all cases.

Figure 18(a) plots the pitching moment coefficient C_M versus C_L for the three horizontal tail configurations and the tail-off configuration. As per aerodynamic convention C_M is plotted negative to the right along the x-axis. Note that the trimmed configuration is not plotted since in this case it simply would produce a constant zero moment. The most negative pitching moments are produced by the $iH = +2^o$ tail setting, while the most positive values are produced by the $iH = -2^o$ tail setting, as expected, with the tail-off configuration falling between the $iH = -2^o$ and $iH = -2^o$ settings. The slope of the curve for the tail-off configuration is $-\frac{\partial C_M}{\partial C_L} = 0.123$ while the slopes of the curves for the three tail-on configurations are approximately $-\frac{\partial C_M}{\partial C_L} = 0.271$. The moment curves all break to the left (unstable) within the range $C_L = 0.55$ to $C_L = 0.62$ which corresponds to the incidence range 3° to 4° as seen in the lift-slope curves.

Figure 18(b) depicts the computed downwash angle at the horizontal tail. This is obtained by interpolating the tail setting which produces the same lift as the tail-off configuration and can be thought of as lining up the symmetric tail sections with the local flow angle. The downwash angle is seen to range from just over 2 degrees at the low C_L conditions to 5 degrees at $C_L = 0.65$

The trim drag and horizontal tail trim angle are plotted in Figure 20. The trim drag is defined as

American Institute of Aeronautics and Astronautics

the difference between the drag of the trimmed configuration and that of the tail-off configuration. The trim angle is defined as the horizontal tail setting that results for the trimmed condition (zero net pitching moment). The trim drag is given as a drag polar form for the drag increment, and the trim angle is plotted along the same vertical C_L scale. The drag increment between these two configurations ranges from 4.8 counts at the low C_L range to 41 at the high C_L range of the plot, while the trim angle varies within the approximate range -0.75^o to $+1^o$ with the value at the nominal $C_L = 0.5$ condition predicted as -0.45^o. These values are in reasonable agreement with the mean collective results reported in the workshop.

Figure 19 illustrates the computed surface pressures and oil flow patterns on the wing and tail surfaces at the Mach=0.85 and 4 degrees incidence case, after the break in the lift and moment slope curves. The flow pattern shows substantial separation on the wing surface aft of the shock location, while flow over the horizontal tail appears to remain mostly attached.
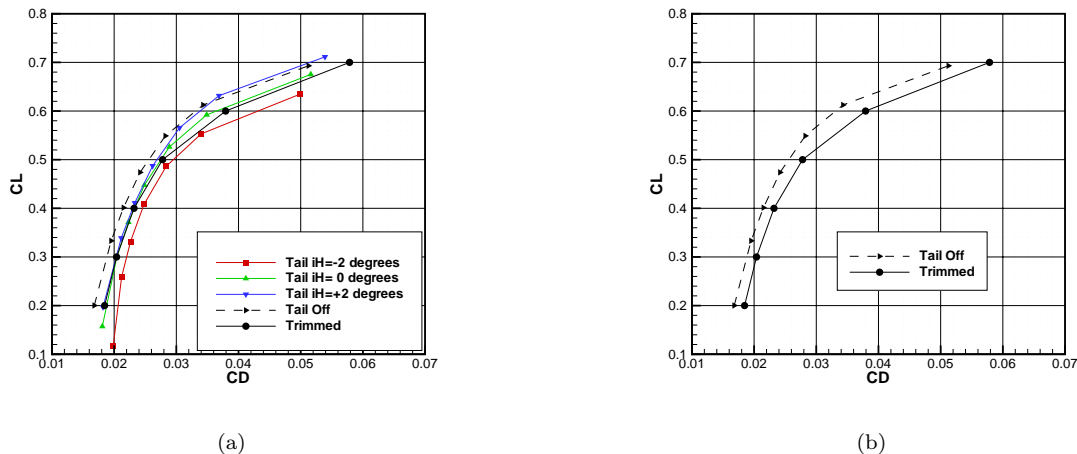

(a)

(b)

Figure 15. Computed drag polar for various CRM tail configurations at Mach=0.85
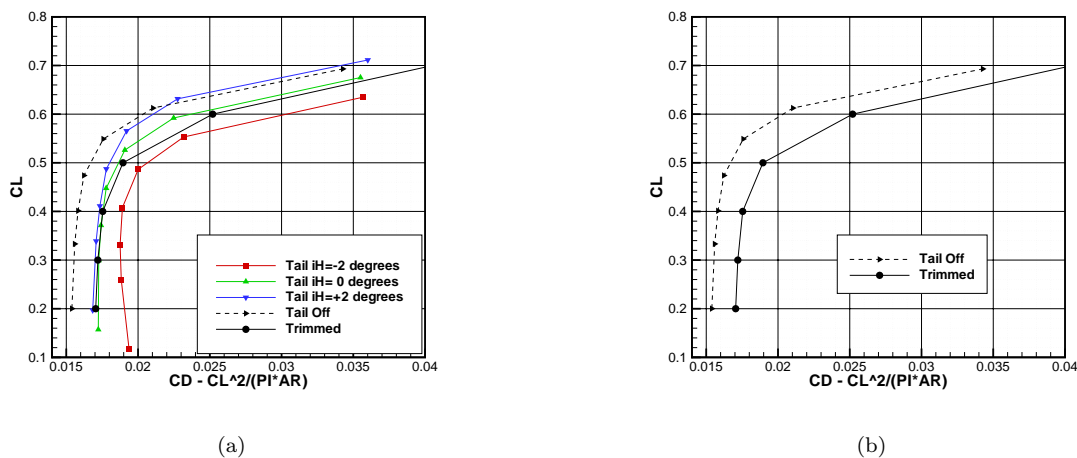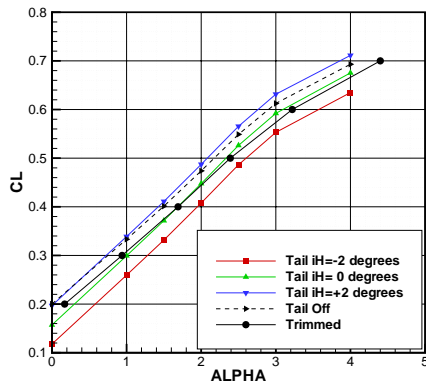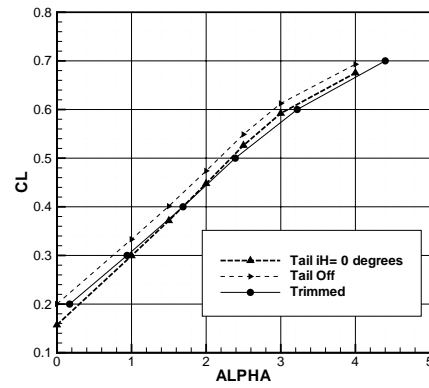
.

(a)

(b)

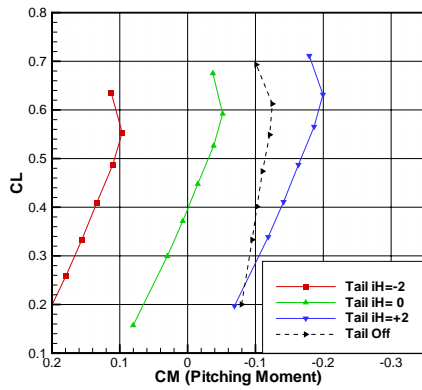Figure 16. Idealized drag polars for various CRM tail configurations at Mach=0.85

.

American Institute of Aeronautics and Astronautics

(a)   (b)
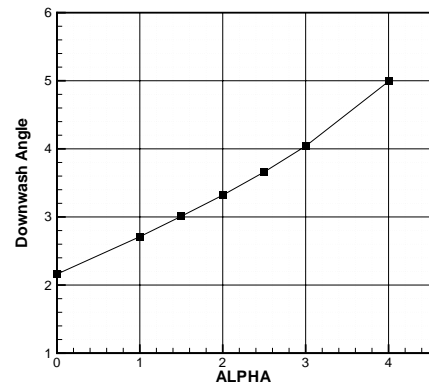
Figure 17. Lift slope curves for various CRM tail configurations at Mach=0.85

.

(a)   (b)

Figure 18. (a) Lift versus incidence curves for various tail settings and (b) computed downwash angle for CRM configuration at Mach=0.85 and Re= 5 million
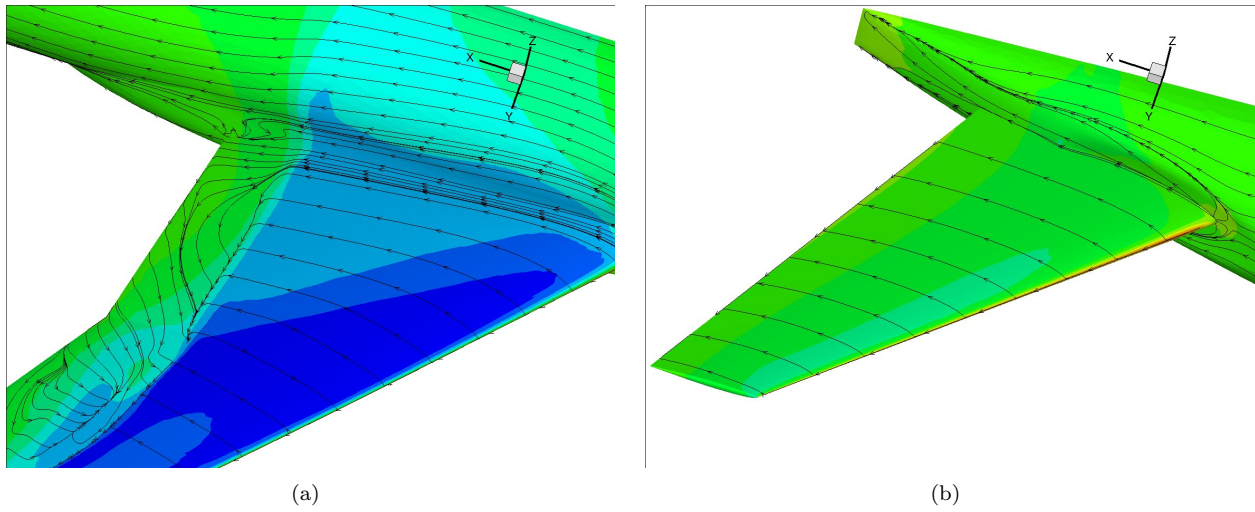
.

(a)	(b)

Figure 19. Computed surface oil flow patterns on (a) wing and (b) tail surfaces for CRM configuration at Mach=0.85 and Re= 5 million and 4 degrees incidence showing shock-induced separation on main wing and attached flow on tail

.

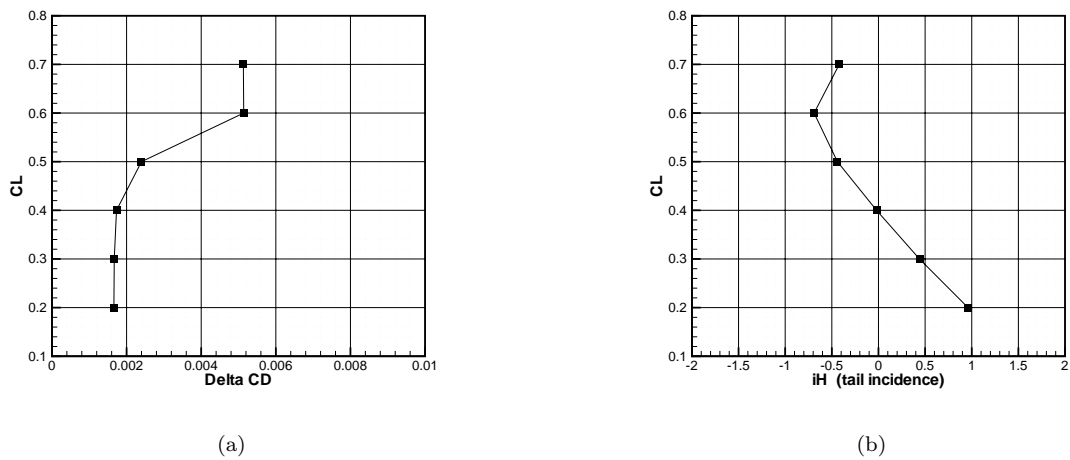|	
(a)	(b)

Figure 20. (a) Computed trim drag as a function of C_L and (b) horizontal tail angle at trim for CRM configuration at Mach=0.85 and Re= 5 million

.

American Institute of Aeronautics and Astronautics

C.   Case 2: Drag Rise Study

The second test, which was optional for the workshop, consists of a drag rise study. This is performed by running a Mach sweep at several fixed C_L conditions on the medium grid for the baseline wing-body-horizontal configuration with the horizontal tail setting of 0°. A total of seven Mach numbers and three C_L conditions were specified for this study. The drag rise curves can be constructed either by running alpha sweeps at fixed Mach conditions and then interpolating the resulting polars to obtain fixed C_L versus Mach number curves, or by computing the points on the drag rise curve directly using the C_L driver for the fixed C_L conditions. In this work, the drag rise curves were constructed in the latter manner, using the C_L driver for generating fixed C_L conditions. The complete group of polars at different Mach numbers computed for this study are shown in Figure 21(a). The drag rise curves are depicted in Figure 21(b), for the three fixed C_L conditions of $C_L = 0.4, 0.45, 0.5$. Defining the drag rise point as the location where the drag increases 20 counts over the corresponding Mach $= 0.7$ value leads to drag rise Mach numbers of 0.87, 0.86 and 0.855 for the three C_L conditions of $C_L = 0.4, 0.45, 0.5$, respectively. These values are in agreement with the design drag cruise Mach number of 0.85 for the CRM wing-body-horizontal configuration.[23]
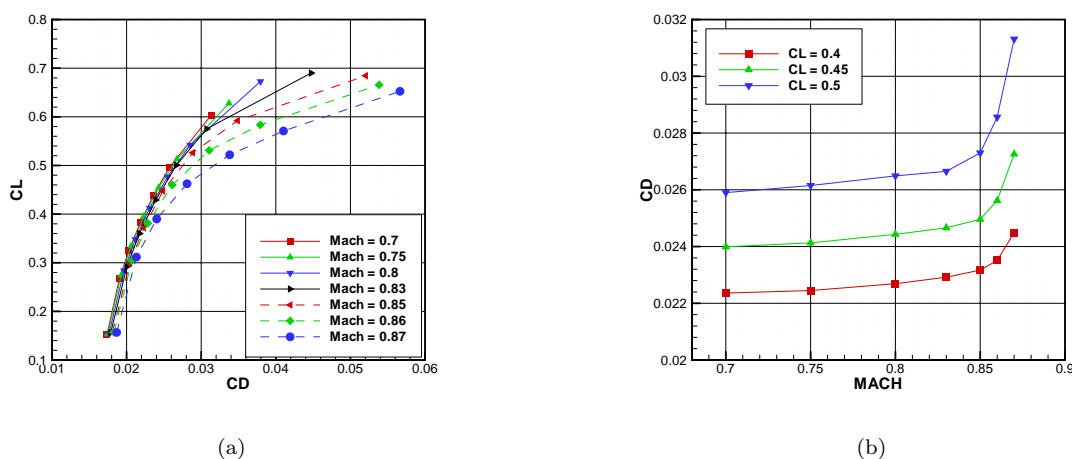

(a)

(b)

Figure 21. (a) Drag polars computed for various Mach numbers and (b) Drag rise curves for CRM with tail at $iH = 0^o$ at Re=5 million

D.   Case 3: Reynolds Number Study

The third test case, which also was optional for the workshop, consists of a Reynolds number effect study on the CRM wing-body-horizontal configuration with a horizontal tail setting of 0°. This case was motivated by the ability to obtain experimental data at different Reynolds numbers in the NTF. The freestream conditions are Mach=0.85, C_L=0.5, and the Reynolds numbers are 5 million and 20 million. The higher Reynolds number case requires the use of a mesh with finer normal spacing at the aircraft surfaces, in order to maintain adequate resolution for accurately predicting skin friction in the thinner boundary layer regions that are associated with the higher Reynolds number case. For this reason, the Re=20 million case was run on a modified grid with tighter boundary layer resolution but similar steamwise and spanwise resolution to the medium mesh used for the previous computations at the lower Reynolds number of 5 million. This additional mesh is described in Tables 1 and 2. For comparison purposes, the high Reynolds number case was also run on the baseline mesh used for the Re=5 million case, providing a measure of grid sensitivity effects for this study. The change in the computed values between the low and high Reynolds numbers cases are given in Table 3, along with the changes in incidence required to hold the fixed C_L condition. The total drag decreases by 32.9 counts in going from Re=5 million to Re=20 million, with approximately one third of this due to pressure drag decrease, and two thirds due to decrease in friction drag. Notably, the pitching moment also becomes more negative for the higher Reynolds number case. These findings are consistent with those reported by other workshop participants.[23] Note that if the same grid is used to compute the high and low Reynolds number cases, the change in drag differs by about 2 counts, which is almost all attributable to

American Institute of Aeronautics and Astronautics

under-estimation of the decrease in friction drag. This is consistent with the notion that friction drag is the force component most directly affected by normal grid spacing in boundary layer regions.

Table 3. Reynolds number study results

Reynolds Number	$Alpha$	CL	CD	CD_p	CD_v	CM
5 million	2.330	0.5000	0.02731	0.01501	0.01230	-0.03064
20 million (same grid)	2.141	0.5000	0.02423	0.01384	0.01039	-0.03649
Delta	-0.189	0.0000	-0.00308	-0.00117	-0.00191	-0.00585
20 million (high Re grid)	2.144	0.5000	0.02402	0.01389	0.01013	-0.03578
Delta	-0.186	0.0000	-0.00329	-0.00112	-0.00217	-0.00514

VI. Conclusions

A complete set of results for the fourth drag prediction workshop have been reported using the NSU3D unstructured mesh Reynolds-averaged Navier-Stokes solver. Results include a grid refinement study, a down-wash study, a drag rise study and a Reynolds number effect study. A drag decomposition study was included in the grid refinement study, and selected cases have been run with two different turbulence models and different discretizations. The reported results have been found to lie close to the mean of the collective workshop results in most cases. In future work we anticipate detailed comparison of these numerical results with experimentally obtained data on the CRM configuration as they becomes available.

VII. Acknowledgments

References

[1]Vassberg, J. C., DeHaan, M. A., Rivers, S. M., and Wahls, R. A., "Development of a Common Research Model for Applied CFD Validation Studies," AIAA Paper 2008-6919.

[2]Rivers, S. M. and Dittburner, A., "Experimental Investigations of the NASA Common Research Model," AIAA Paper 2010-4218.

[3]Levy, D. W., Zickuhr, T., Vassberg, J., Agrawal, S., Wahls, R. A., Pirzadeh, S., and Hemsch, M. J., "Summary of Data from the First AIAA CFD Drag Prediction Workshop," AIAA Paper 2002-0841.

[4]Laflin, K., Brodersen, O., Rakowitz, M., Vassberg, J., Wahls, R., and Morrison, J., "Summary of Data from the Second AIAA CFD Drag Prediction Workshop," AIAA Paper 2004-0555.

[5]Vassberg, J. C., Tinoco, E. N., Mani, M., Brodersen, O. P., Eisfeld, B., Wahls, R. A., Morrison, J. H., Zickuhr, T., Laflin, K. R., and Mavriplis, D. J., "Summary of the Third AIAA CFD Drag Prediction Workshop," AIAA Paper 2007-0260.

[6]Mavriplis, D. J., "Third Drag Prediction Workshop Results using the NSU3D Unstructured Mesh Solver," *AIAA Journal of Aircraft*, Vol. 45, No. 3, May 2008, pp. 750–761.

[7]"First AIAA High Lift Prediction Workshop." Chicago, IL. http://highliftpw.larc.nasa.gov.

[8]Mavriplis, D. J. and Levy, D. W., "Transonic Drag Prediction using an Unstructured Multigrid Solver," *AIAA Journal of Aircraft*, Vol. 42, No. 4, 2003, pp. 887–893.

[9]Lee-Rausch, E. M., Buning, P. B., Mavriplis, D. J., Morrison, J. H., Park, M. A., Rivers, S. M., and Rumsey, C. L., "CFD Sensitivity Analysis of a Drag Prediction Workshop Wing/Body Transport Configuration," AIAA Paper 2003-3400.

[10]Lee-Rausch, E. M., Frink, N. T., Mavriplis, D. J., Rausch, R. D., and Milholen, W. E., "Transonic Drag Prediction on a DLR-F6 Transport Configuration using Unstructured Grid Solvers," AIAA Paper 2004-0554.

[11]Mavriplis, D. J., "Aerodynamic Drag Prediction Using Unstructured Mesh Solvers," *CFD-Based Drag Prediction and Reduction, eds. H. Deconoinck, K. Sermus and C. van Dam, VKI Lecture Series 2003-02, von Karman Institute for Fluid Dynamics, Rhode St-Genese, Belgium*, March 2003.

[12]Mavriplis, D. J., "Grid Resolution Study of a Drag Prediction Workshop Configuration Using the NSU3D Unstructured Mesh Solver," AIAA-Paper 2005-4729.

[13]Mavriplis, D. J. and Venkatakrishnan, V., "A Unified Multigrid Solver for the Navier-Stokes Equations on Mixed Element Meshes," *International Journal for Computational Fluid Dynamics*, Vol. 8, 1997, pp. 247–263.

[14]Spalart, P. R. and Allmaras, S. R., "A One-equation Turbulence Model for Aerodynamic Flows," *La Recherche Aérospatiale*, Vol. 1, 1994, pp. 5–21.

[15] Wilcox, D. C., "Re-assessment of the scale-determining equation for advanced turbulence models," *AIAA Journal*, Vol. 26, 1988, pp. 1414–1421.

[16] Menter, F. R., "Two-Equation Eddy-Viscosity Turbulence Models for Engineering Applications," *AIAA Journal*, Vol. 32, No. 8, 1994, pp. 1598–1605.

[17] Mavriplis, D. J., "Multigrid Strategies for Viscous Flow Solvers on Anisotropic Unstructured Meshes," *Journal of Computational Physics*, Vol. 145, No. 1, Sept. 1998, pp. 141–165.

[18] Mavriplis, D. J. and Pirzadeh, S., "Large-Scale Parallel Unstructured Mesh Computations for 3D High-Lift Analysis," *AIAA Journal of Aircraft*, Vol. 36, No. 6, Dec. 1999, pp. 987–998.

[19] Mavriplis, D. J. and Yang, Z., "Construction of the Discrete Geometric Conservation Law for High-Order Time Accurate Simulations on Dynamic Meshes," *Journal of Computational Physics*, Vol. 213, No. 1, April 2006, pp. 557–573.

[20] Yamazaki, W., , Matsushima, K., and Nakahashi, K., "Application of Drag Decomposition Method to CFD Computation Results," AIAA Paper 2005-4723.

[21] Yamazaki, W., , Matsushima, K., and Nakahashi, K., "Aerodynamic Optimization using the Drag Decomposition Method," *AIAA Journal*, Vol. 46, No. 5, 2008, pp. 1096–1106.

[22] Mavriplis, D. J., Vassberg, J. C., Tinoco, E. N., Mani, M., Brodersen, O. P., Eisfeld, B., Wahls, R. A., Morrison, J. H., Zickuhr, T., and Levy, D., "Grid Quality and Resolution Issues from the Drag Prediction Workshop Series," AIAA Paper 2008-0930.

[23] Vassberg, J. C., Tinoco, E. N., Mani, M., Zickuhr, T., Levy, D., Brodersen, O. P., Eisfeld, B., Wahls, R. A., Morrison, J. H., Mavriplis, D. J., and Murayama, M., "Summary of the Fourth AIAA CFD Drag Prediction Workshop," AIAA Paper 2010-4547.